Astronomy & Astrophysics manuscript no. aanda
December 21, 2023
©ESO 2023

Detecting exoplanets in reflected ligth from the ground

Fondamental limits of dual field interferometry

S. Lacour[1], Oscar[2,⋆], and ...?

[1] Institute for Astronomy (IfA), University of Vienna, Türkenschanzstrasse 17, A-1180 Vienna
e-mail: wuchterl@amok.ast.univie.ac.at
[2] University of Alexandria, Department of Geography, ...
e-mail: c.ptolemy@hipparch.uheaven.space ⋆⋆

Received September 15, 1996; accepted March 16, 1997

ABSTRACT

Aims.
Methods.
Results.

Key words. – – –

1. Introduction

The direct-imaging technique has been identified as a priority to characterize exoplanet by community reports and space agencies, including the US Astro 2020 Decadal Survey (National Academies of Sciences Engineering and Medicine 2021) and ESA's Voyage 2050 Senior Committee report. The reason is that many important molecular (bio)signatures are low in the atmosphere making them very difficult to observe by transit spectroscopy (Lustig-Yaeger, Jacob 2019). Thus, multiple direct-imaging space observatories have been proposed. In the near term, the Coronagraph Instrument aboard the Nancy Grace Roman Space Telescope (Spergel et al. 2015) should be the first instrument to detect reflected light from space. In the longer term the next US flagship mission should be the Habitable Worlds Observatory, based on the LUVOIR (The LUVOIR Team 2019) and HabEx (Gaudi et al. 2020) preparatory studies. In Europe, a significant momentum push toward a mid-infrared optical interferometer called LIFE (Quanz et al. 2021), this time targeting thermal emission.

But what can exoplanets be detected from the ground? The advantages of ground-based observatories are the large collecting apertures, as well as a significantly higher angular resolution. The disadvantages are the thermal background, and both atmospheric and quasi-static aberrations which makes post-processing deconvolution difficult. Nevertheless, several exoplanets have been successfully discovered and directly imaged from the ground. These detected exoplanets are massive and young exoplanets. Their mass and ages make there are still cooling off, slowly disipating the gravitational energy amassed during formation. Thus, they are still hot: 1700K for beta Pictoris b, down to 800K for 51 Eri b. This is why, thanks to their thermal emission, they are still relatively bright compared to their star with contrast ratios of the order of a few 10^{-5}. However, the vast majority of known and unknown planets are colder, at equilibrium temperature with the irradiation of their stellar host. These objects self-emit in mid-infrared wavelength, but at near infrared wavelength, only the reflected stellar light can be seen, although very faint. This reflected stellar light is then of the order of 1e-8 or even lower, with a strong dependance on the semi-major axis of the planet.

With these levels of contrast in mind, can exoplanets be detected in reflected light from the ground? In a key paper, Guyon (2005) summary the challenges faced. The first issue is the atmosphere. With a single dish telescope, they are reduced by using an adaptive optics system (eg, SPHERE extreme AO, Beuzit et al. 2019). Experience show that the atmospheric halo averages rapidly: it is not a main problem by itself apart for the extra photon noise that it produces off axis. The second issue is the diffraction pattern. The diffraction pattern can also be well calibrated, although it also brings additional photon noise. It can reduced by a coronagraph (eg, Rouan et al. 2020). The third one is the non-common path quasi-static aberrations, which produce slow moving speckles that are difficult to calibrate. It is currently the most difficult issue. A 1e-5 speckle to be stable at 1% would require a wavefront stable within 4pm (at 1.6um, Guyon 2005). These speckles can be reduced using post-processing techniques like SDI (eg, Racine et al. 1999) or ADI (eg, Marois et al 2000). They can be reduced in real time by focal plane wavefront sensing and real time correction (eg, the dark-hole technique, Potier et al. 2020). However, to do so, the wavefront must be stable enough to allow that during the sensing time: if the speckle moves faster than it takes to detect it, it cannot be removed. This is what makes Guyon (2005) come in substance with the conclusion that Earth-size planet could not be detectable from the ground around solar type stars.

If a single dish telescope does not work, could optical interferometry be a solution? The goal is not anymore to sense the details of the electric field over a 8-meter aperture, but to work with the electric field once coupled into a single mode

⋆ Just to show the usage of the elements in the author field
⋆⋆ The university of heaven temporarily does not accept e-mails

fiber. More exactly, the exoplanet signal is then seen as a coherent signal between the electric field of the two telescopes, with the stellar speckle affecting the coherent signal with a very different signature, so much that it can be filtered out without necessarely being detected at the level of the exoplanetary signal. This is at the core of several ideas for high contrast instruments at the VLTI, that can be divided into 2 main types: the single field and dual field interferometry. In single field interferometry, distinguishing the coherent signal from the star and the exoplanet is obtained using thechniques likes closure phase, nulling (eg. Bracewell nuller, 1978), or a combination of the two techniques like Kernel nulling (Martinache & Ireland, 2018, Chingaipe et al. 2023).

But recently, it is a dual field optical interferometer (Gravity collaboration et al. 2017) which happended to be the first interferometric technique to directly detect an exoplanet (Gravity collaboration et al. 2019). A dual field interferometer works by observing simulatenously 2 narrow field of view typically of the size of the telescope point spread function. These 2 fields are within a large field of view that can be of several arcseconds, including, in our case, a star and an exoplanet (figure 1). The advantage is that one interferemeter can observe the star, while the other can observe the exoplanet. This means that the photon noise of the star will not contaminate too much the exoplanet signal, because the stellar light is filtered by the narrow field of view of the inteferometer. This has been key to the observations of 2 short separation exoplanets: Beta Pictoris c (Nowak et al. 2020) and HD206893 c (Hinkley et al. 2023).

In this paper, we investigate the capacity of a dual field optical interferometer to detect the reflected light of an exoplanet. The theoretical achievable snr is presented in section 2. The detection level is then calculated on known RV exoplanets in section 3. In section 4, we conclude.

2. Simulation of contrast range

2.1. The detection principle

We simulated a 2 telescopes interferometer, with 8 meters telescopes, observing in the J band (1-1.2 microns). The hypothesis is 2 independent telescopes, with 2 independant atmospheric perturnations corrected by adaptive optics. The parameters, as a function of $\boldsymbol{u}$ the X-Y coordinate vector in meter inside the pupil, are:

- $\mathsf{A}_T(\boldsymbol{u})$: the amplitude aberration of the electric field,
- $\Phi_T(\boldsymbol{u})$: the residual atmospheric phase aberrations.
- $\Psi_\alpha(\boldsymbol{u})$: An apodizing phase mask, optimized for a separation $\boldsymbol{\alpha}$ between the 2 interferometers.

Hence, the electric field inside the pupil of telescope T writes:

$$\mathsf{W}_T(\boldsymbol{u}) = \mathsf{O}(\boldsymbol{u})\mathsf{A}_T(\boldsymbol{u})\exp(i\Phi_T(\boldsymbol{u}) + i\Psi_\alpha(\boldsymbol{u})) \quad (1)$$

Were $\mathsf{O}(\boldsymbol{u})$ is the incoming field of the astronomical object in the pupil of each telescope. Its amplitude depends on the magnitude of the object, and its phase depends on the position of the object on the sky.

Injecting into Eq. (1) $\mathsf{S}_\star$ and $\mathsf{S}_\oplus$, the amplitude of the incoming electric field per unit of collecting aera of respectively the star and the exoplanet, and assuming the star is observed on-axis as represented in Fig.1, and the exoplanet off-axis, the resulting electic field inside the pupil plane of each telescopes now write, for the star and the planet:

$$\mathsf{W}_{T_1,\star}(u) = \mathsf{S}_\star\mathsf{A}_{T_1}(\boldsymbol{u})\exp(i\left[\Phi_{T_1}(\boldsymbol{u}) + \Psi_\alpha(\boldsymbol{u})\right]) \quad (2)$$

$$\mathsf{W}_{T_2,\star}(u) = \mathsf{S}_\star\mathsf{A}_{T_2}(\boldsymbol{u})\exp(i\left[\Phi_{T_2}(\boldsymbol{u}) + \Psi_\alpha(\boldsymbol{u})\right]) \quad (3)$$

$$\mathsf{W}_{T_1,\oplus}(u) = \mathsf{S}_\oplus\mathsf{A}_{T_1}(\boldsymbol{u})\exp(i\left[\Phi_{T_1}(\boldsymbol{u}) + \Psi_\alpha(\boldsymbol{u}) + k\boldsymbol{\alpha}\cdot\boldsymbol{u}\right]) \quad (4)$$

$$W_{T_2,\oplus}(u) = \mathsf{S}_\oplus A_{T_2}(\boldsymbol{u})\exp(i\left[\Phi_{T_2}(\boldsymbol{u}) + \Psi_\alpha(\boldsymbol{u}) + k\boldsymbol{\alpha}\cdot(\boldsymbol{B}+\boldsymbol{u})\right]) \quad (5)$$

Where k is the wavenumber, $\boldsymbol{\alpha}$ is the vector position of the stellar object with respect to the planet, while $\boldsymbol{B}$ is the narrow angle baseline vector [1]. The dot operator is the scalar product, hence $\boldsymbol{\alpha}\cdot\boldsymbol{B}$ corresponds to an optical path delay bewteen the two telescopes. $W_(u) = 0$ outside of the telescope pupil. The subscript $\star$ to denote the star and $\oplus$ for the exoplanet will be kept for the rest of this paper.

The flux injected into one fiber is the projection of the electric field on the mode of the fiber. This projection can be calculated either in the focal plane, or in the Fourier transform of it. This is mathematically equivalent accoriding to the perceval planchet theroem. Moreover, asuming the far field Fraunhofer hypothesis, the Fourier transform of the field plane is the pupil plane. Hence, the electric field injected into a fiber can be calculated from the cross-product integrated over the pupil of the telescope:

$$E = \iint \mathsf{W}(\boldsymbol{u})\mathsf{F}(\boldsymbol{u})^*\, d\boldsymbol{u}\,, \quad (6)$$

where $\mathsf{F}(\boldsymbol{u})$ is the Fourier transform of the fondamental mode of the fiber (the acceptance field of single mode fiber). It can be approximated as a gaussian-shaped mode, caracterized by its beam waist w, defined here in the pupil:

$$E_{T,I_1} = \sqrt{\frac{2}{\pi w^2}}\iint \mathsf{W}_T(\boldsymbol{u})\exp(-\frac{|\boldsymbol{u}|^2}{w^2})\, d\boldsymbol{u} \quad (7)$$

$$E_{T,I_2} = \sqrt{\frac{2}{\pi w^2}}\iint \mathsf{W}_T(\boldsymbol{u})\exp(-\frac{|\boldsymbol{u}|^2}{w^2} - ik\boldsymbol{\alpha}\cdot\boldsymbol{u})\, d\boldsymbol{u} \quad (8)$$

for respectively the first and second interferometer. On the first interferometer, the single mode fiber point on axis in the direction of the stellar light. For the second interferometer, pointing off axis toward the planetary companion, the fondamental mode of the single mode fiber in the pupil writes with a phase tilt $k\boldsymbol{\alpha}\cdot\boldsymbol{u}$. The width of the gaussian shape in the pupil plane (w) is optically adjusted to maximize the injection of non-aberrated starlight ($w = 0.446 \times D$ for a circular un-obstructed aperture).

To summary, we have 8 electric field: 2 for each telescopes, and 2 for each interferometers, and 2 for each targets. They are summarized in Table 1.

The interference patterns will be observed simultaneously on the 2 interferometers, as a function of an internal, well calibrated, optical delay x[2]:

$$I_1(x) = |E_{T_1,I_1,\star}|^2 + |E_{T_2,I_1,\star}|^2 + 2\Re\left[\langle E_{T_1,I_1,\star}E^*_{T_2,I_1,\star}\rangle\exp(i\,x)\right] \quad (9)$$

$$I_2(x) = |E_{T_1,I_2,\star}|^2 + |E_{T_2,I_2,\star}|^2 + |E_{T_1,I_2,\oplus}|^2 + |E_{T_2,I_2,\oplus}|^2 + 2\Re\left[\left(\langle E_{T_1,I_2,\star}E^*_{T_2,I_2,\star}\rangle + \langle E_{T_1,I_2,\oplus}E^*_{T_2,I_2,\oplus}\rangle\right)\exp(i\,x)\right] \quad (10)$$

[1] for a precise definition of the narrow angle baseline, please see the Woillez & Lacour 2018 paper.

[2] Specifically, GRAVITY is using an ABCD beam combiner, which means x consist in four delay at 0, $\pi/2$, π, and $3\pi/2$ radians.

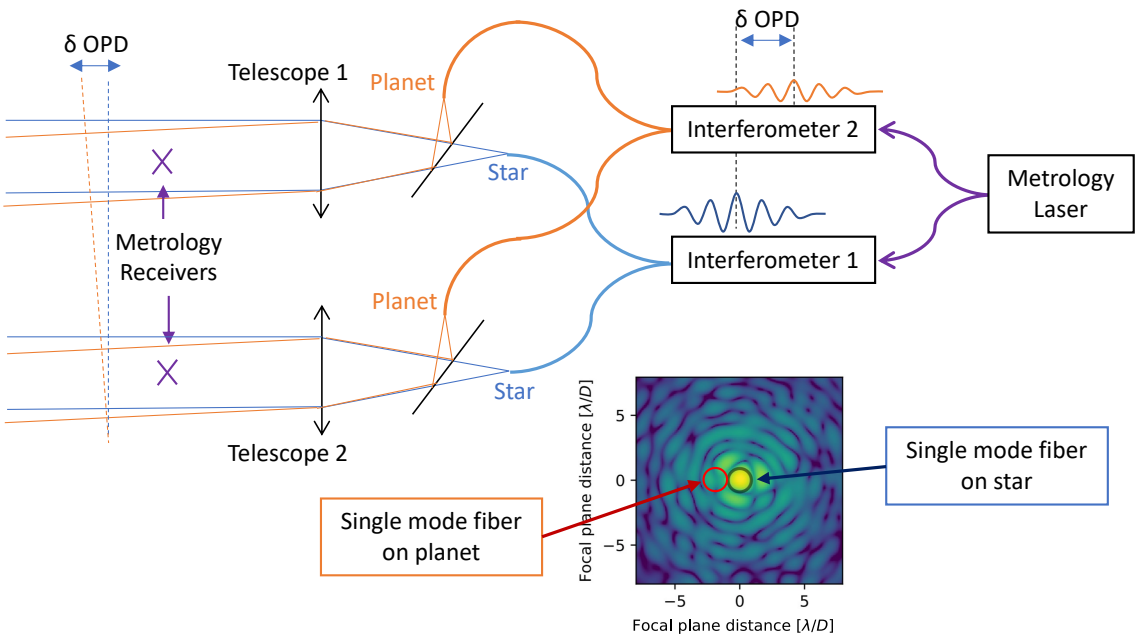

Fig. 1. Schematic diagram of a two telescopes dual field optical interferometer. A beam splitter is used to make 2 images of the focal plane where two fibers are situated. One fiber is positioned on the star itself and the flux used to feed interferometer 1, which serves as reference for the phase. The other fiber is positionned on the exoplanet, and feeding interferometer 2. The exoplanet is detected as a coherent flux on interferometer 2, shifted with respect to the stellar coherent flux by an optical path delay δOPD equivalent to the scalar product between the astrometric baseline vector $\boldsymbol{B}$ and the angular separation between the star and the exoplanet $\boldsymbol{\alpha}$.

Table 1. The four electric fields in the fibers of a dual field interferometer. The upper table correspond to the electric field of the star, and the lower part of the table correspond to the electric field of the planet.

	Interferometer 1	Interferometer 2
Telescope 1	$E_{T_1,I_1,\star} = \sqrt{\frac{2}{\pi w^2}} \iint \mathsf{S}_\star \exp\left(-\frac{\lvert\boldsymbol{u}\rvert^2}{w^2} + i\Phi'_{T_1}(\boldsymbol{u})\right) d\boldsymbol{u}$	$E_{T_1,I_2,\star} = \sqrt{\frac{2}{\pi w^2}} \iint \mathsf{S}_\star \exp\left(-\frac{\lvert\boldsymbol{u}\rvert^2}{w^2} + i(\Phi'_{T_1}(\boldsymbol{u}) - k\boldsymbol{\alpha}\cdot\boldsymbol{u})\right) d\boldsymbol{u}$
Telescope 2	$E_{T_2,I_1,\star} = \sqrt{\frac{2}{\pi w^2}} \iint \mathsf{S}_\star \exp\left(-\frac{\lvert\boldsymbol{u}\rvert^2}{w^2} + i\Phi'_{T_2}(\boldsymbol{u})\right) d\boldsymbol{u}$	$E_{T_2,I_2,\star} = \sqrt{\frac{2}{\pi w^2}} \iint \mathsf{S}_\star \exp\left(-\frac{\lvert\boldsymbol{u}\rvert^2}{w^2} + i(\Phi'_{T_2}(\boldsymbol{u}) - k\boldsymbol{\alpha}\cdot\boldsymbol{u})\right) d\boldsymbol{u}$
Telescope 1	$E_{T_1,I_1,\oplus} \approx 0$	$E_{T_1,I_2,\oplus} = \sqrt{\frac{2}{\pi w^2}} \iint \mathsf{S}_\oplus \exp\left(-\frac{\lvert\boldsymbol{u}\rvert^2}{w^2} + i\Phi'_{T_1}(\boldsymbol{u})\right) d\boldsymbol{u}$
Telescope 2	$E_{T_2,I_1,\oplus} \approx 0$	$E_{T_2,I_2,\oplus} = \sqrt{\frac{2}{\pi w^2}} \iint \mathsf{S}_\oplus \exp\left(-\frac{\lvert\boldsymbol{u}\rvert^2}{w^2} + i(\Phi'_{T_2}(\boldsymbol{u}) + k\boldsymbol{\alpha}\cdot\boldsymbol{B})\right) d\boldsymbol{u}$

Notes. The intration domain is the size of the pupil. This table assume $A_T(\boldsymbol{u}) = 1$ and it is using $\Phi'_T(\boldsymbol{u}) = \Phi_T(\boldsymbol{u}) + \Psi_\alpha(\boldsymbol{u})$. The vector $\boldsymbol{B}$ is the astrometric baseline vector and $\boldsymbol{\alpha}$ the angle between star and planet on sky. $\mathsf{S}_\star$ and $\mathsf{S}_\oplus$ are the amplidute of incoming electric field for respectively the star and the exoplanet.

Here, the exoplanetary light entering interferometer 1 is assumed to be negligeable, so the only coherent energy, $\langle E_{T_1,I_1,\star} E^*_{T_2,I_1,\star}\rangle$, originate from the star. The exoplanetary signal $\langle E_{T_1,I_2,\oplus} E^*_{T_2,I_2,\oplus}\rangle$ is observable in interferometer 2, but blended with the fringes of stellar origin, $\langle E_{T_1,I_2,\star} E^*_{T_2,I_2,\star}\rangle$. By analogy with direct imaging, we call in this paper these fringe of stellar origin "coherent speckle". The goal is therefore to retreive the exoplanetary signal in interferometer 2 by filtering out the stellar coherent speckle.

A generalisation to an unlimited number of telescopes can be done to estimate the signal to noise of the exoplanet detection for any number of telescope. It can then be written as:

$$snr = \frac{S_\oplus A_\oplus^{\text{apod}} A_\oplus^{\text{processing}}}{\sqrt{N^2_{\text{readout}} + N^2_{\text{background}} + N^2_{\text{stellar photons}} + N^2_{\text{speckle}}}} \tag{11}$$

where $S_\oplus$ is the signal of the planet. For a given telescope, it is equivalent to the intensity entering the pupil:

$$S_\oplus = \iint \|\mathsf{S}_\oplus\|^2 \, d\boldsymbol{u} \,. \tag{12}$$

This signal is decreased by $A_\oplus^{\text{apod}}$ because of the apodizer, and decreased by $A_\oplus^{\text{processing}}$ due to the filtering of the coherent speckles. In the case of the single baseline interferometer described above, $S_\oplus A_\oplus^{\text{apod}}$ correspond to the amplitude of the exoplanetary fringes:

$$S_\oplus A_\oplus^{\text{apod}} = \left\|\langle E_{T_1,I_2,\oplus} E^*_{T_2,I_2,\oplus}\rangle\right\| \tag{13}$$

This term is described in more details in section 2.3.

The other attenuation term, $A_\oplus^{\text{processing}}$, is here to account for the fact that the exoplanet fringes is mixed with coherent speckles. Therefore a deconvolution process is applied to the observed

Table 2. Simulation parameters

	Fig. 2	Fig. 3	Fig. 4	Fig. 5
$F_\star$	10 Jy	10 Jy		10 Jy
$\Delta\lambda/\lambda$	0.23	0.23	0.23	0.23
δt	100 s	100 s		100 s
Δt	10 000 s	10 000 s		10 000 s
$N_{\rm tel}$	4	4	2	4
D	8	8	8	8
T	0-10%	5%		5%
R	100	100	100	100
λ	J/H/K/L	K	K	I/J/H/K/L
Strehl		85/95	85	85/95/98
$\lvert\boldsymbol{B}\rvert$			50/100 m	50/100/250 m
$N_{\rm poly}$			4-8-12	12

fringe pattern, which decreases the amplitude of the exoplanetary signal that is observed. The term $A_\oplus^{\rm processing}$ can only be described as a function of the speckle removing technique, which is described in section 2.4.

The different source of noise, in the numerator, are caused mostly by classical sources of noise: the detector readout ($N_{\rm readout}$), the photon noise of the thermal background ($N_{\rm background}$), and the photon noise caused by the remaining starlight $N_{\rm stellar\ photons}$. A last source of noise, $N_{\rm speckle}$, comes from the residual coherent energy of the speckle after post processing.

2.2. Readout and background noise

The amplitude of the exoplanetary signal depends on the flux emmited by the exoplanet $F_\oplus$, the bandpass of the interferometer $\Delta\lambda/\lambda$, the duration of the integration Δt, the number and size of the telescopes (N and D), and the transmission of the interferometer T.

$$S_\oplus = F_\oplus \frac{\Delta\lambda}{\lambda} \Delta t\, N_{\rm tel} \frac{\pi D^2}{4} T\,. \tag{14}$$

On the other hand, the read-out noise of the detector depends purely on the detector caracteristic, as well as the number of pixels read. It can be written as:

$$N_{\rm readout} = \sigma_{e^-} \sqrt{4\, \frac{N_{\rm tel}(N_{\rm tel}-1)}{2}\, \frac{3R\Delta\lambda}{\lambda}\, \frac{\Delta t}{\delta t}} \tag{15}$$

where the value under the square root correspond to the total number of reads during the full observation. The value $N_{\rm tel}(N_{\rm tel}-1)/2$ corresponds to the number of baselines recombined, R is the spectral resolution over-sampled by a factor 3, and the factor 4 correspond to the number of pixels per baseline needed for an ABCD recombination scheme. The individual frame integration time is Δt, hence the ratio $\delta t/\Delta T$ correspond to the number of frames taken. On the most recent Teledyne H2RG detectors, σ_{e^-} is typically of the order of 5 photo-electrons in a Fowler-16 detection readout scheme.

The thermal background noise $N_{\rm background}$ can be estimated assuming that the black body emmission from the laboratory dominate the emmission. This approximation is especially valid in light of the low throughput of the optical chain of the interferometer ($T < 10\,\%$). The background emmission can then be analytically estimated using the limited accepetance angle of a single mode fiber:

$$N_{\rm background} = \sqrt{N_{\rm tel}(1-T)\, \frac{\Delta\lambda}{\lambda}\, \lambda^2\, B_\nu(300\,K, \lambda)\, \Delta t}\,. \tag{16}$$

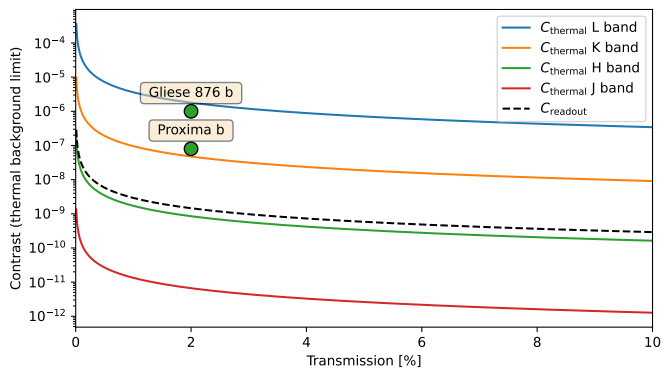

Fig. 2. Contrast limit at the VLTI as a function of the total transmission of the interferometer. The color curves are theoretical contrast curves limited by the thermal background of the laboratory (at 300 K). The dashed curves is the contrast limit from the detector readout noise. The parameters of the simulation are given in Table 2.

In this equation, $B_\nu(300\,K, \lambda)$ is the number of photons emmited by a 300 K black body at the wavelength of observation, λ^2 the etendu of a single mode fiber, and $\Delta\lambda/\lambda$ the bandwith of the interferometer.

To check the impact of these 2 noises on the contrast range, the Eq. (11), which drive the final signal to noise calculation, can be simplified. It then write as the 2 equations:

$$snr_{\rm readout} = \frac{S_\oplus}{N_{\rm readout}} \qquad snr_{\rm thermal} = \frac{S_\oplus}{N_{\rm background}} \tag{17}$$

which can be turned into 2 contrast limits:

$$C_{\rm readout} = \frac{N_{\rm readout}}{S_\star} \qquad C_{\rm thermal} = \frac{N_{\rm background}}{S_\star} \tag{18}$$

where $S_\star$ is calculated similarly to $S_\oplus$:

$$S_\star = F_\star \frac{\Delta\lambda}{\lambda} \Delta t\, N_{\rm tel} \frac{\pi D^2}{4} T \tag{19}$$

Both $C_{\rm readout}$ and $C_{\rm thermal}$ are plotted in Fig. 2 assuming the typical values at the VLTI when observing exoplanets with GRAVITY. These typical values are mentionned in Table 2. Additionally are plotted on the same plot the contrast ratio expected when observing two favorable exoplanets in reflected light: Gliese 876 b and Proxima Centuri b. It can be seen from this plot that having a high tranmission is primordial, if only because of the intrinsic low brightness of the exoplanets. With a typical transmission of 2%, the readout noise starts to limit the detection slightly above 10^{-9}. Last the wavelength of operation inders the observability of reflected light above 3 microns, because of the 300 K emission of the laboratory. At shorter wavelength, the thermal emission equals the detector readout noise near the H band. At even longer wavelength, the step increase of thermal background makes the contrast even more limited. Even though the contrast ratio between planet and star becomes more favorable thanks to the thermal emmision of the planet.

2.3. Starlight suppression

An important objective of high contrast imaging is to suppress as much as possible of the stellar light to decrease the contamination of the signal by photon noise:

$$N_{\rm stellar\ photons} = \sqrt{S_\star A_\star^{\rm apod}} \tag{20}$$

with, in the case of a single interferomter:

$$S_\star A_\star^{\rm apod} = \left\| E_{T,I_2,\star} \right\|^2 \tag{21}$$

which is the flux entering a single mode fiber summed over the wavelength bandpass. This equation is really similar to Eq. (13) except that it correspond to the incoherent flux injected into the fibers instead of the coherent flux observed on the interferometer. From this equation, and using the electric field as described by Table 1, we can derive the attenuation caused by the single mode filtering and the phase apodizer:

$$A_\star^{\rm apod} = \frac{2\left\| \iint \mathsf{S}_\star \exp\left(-\frac{|\boldsymbol{u}|^2}{w^2} + i(\Phi_T(\boldsymbol{u}) + \Psi_\alpha(\boldsymbol{u}) - k\boldsymbol{\alpha}\cdot\boldsymbol{u})\right) d\boldsymbol{u} \right\|^2}{\pi w^2 \iint \|\mathsf{S}_\star\|^2 \, d\boldsymbol{u}} \tag{22}$$

This attenuation of the stellar light $A_\star^{\rm apod}$ decreases the further the exoplanet is from the star (when $\boldsymbol{\alpha}$ increase). For a given separation, this apodization can also be minimized using $\Psi_\alpha(\boldsymbol{u})$, a phase apodizer (eg, Por 2017). It does also decrease with the optical aberrations $\Phi_T(\boldsymbol{u})$, but that does not improve the contrast since the exoplanetary signal is also similarly affected. Indeed, the attenuation that is observed on the exoplanetary light also depends on the optical aberration due to the atmosphere.

Using $A_\oplus^{\rm apod}$ as defined by Eq. (13), and assuming the exoplanetary light to be 100 % coherent (planet not resolved by the interferometer), the apodization $A_\oplus^{\rm apod}$, can be similarly spelled from the equations in Table 2:

$$A_\oplus^{\rm apod} = \frac{2\left\| \iint \mathsf{S}_\oplus \exp\left(-\frac{|\boldsymbol{u}|^2}{w^2} + i(\Phi_T(\boldsymbol{u}) + \Psi_\alpha(\boldsymbol{u}))\right) d\boldsymbol{u} \right\|^2}{\pi w^2 \iint \|\mathsf{S}_\oplus\|^2 \, d\boldsymbol{u}} \tag{23}$$

Therefore, the signal to noise as mentioned in Eq. (11) can be improved by using a phase apodizer which decreases $A_\star^{\rm apod}$ but not $A_\oplus^{\rm apod}$. There are several ways to imagine a phase apodizer, but in this work, we assume we are using a phase apodizor as a prescription applied to the deformable mirror:

$$\Psi_\alpha(\boldsymbol{u}) = k \times OPD_\alpha(\boldsymbol{u}) \tag{24}$$

$$OPD_\alpha(\boldsymbol{u}) = a_\alpha \sin(k_0\boldsymbol{\alpha}\cdot\boldsymbol{u}) + b_\alpha k_0 \boldsymbol{\alpha}\cdot\boldsymbol{u}\cos(k_0\boldsymbol{\alpha}\cdot\boldsymbol{u}) \tag{25}$$

where the optical path different applied by the mirror has 2 degrees of freedom: a_α and b_α which are calculated a posteriori for a given separation $\boldsymbol{\alpha}$. Only one degree of freedom would be necessary to ensure $A_\star^{\rm apod} = 0$ on a very narrow spectral band, but we are using here two degrees of freedom to ensure a broadband attenuation. The wavenumber k_0 is the wavenumer at the center of the bandpass (i.e. $k_0 = 2\pi/2.2\,\mu$m for an observation in the K band). Each parameter $a(|\boldsymbol{\alpha}|)$ and $b(|\boldsymbol{\alpha}|)$ are numerically optimized to minimize $A_\star^{\rm apod}$ over all wavelength, as spelled in Eq. (22). Optimization is done numerically for $\Phi_T(\boldsymbol{u}) = 0$ and $\mathsf{S}_\star = 1$. The resulting values calculated for the pupil of a very large telescope at Paranal is showed in the upper panel of Fig. 3, as a function of $|\boldsymbol{\alpha}|$ in unit of resolution element (λ/D).

In the lower panels of Fig. 3, we show several simulations for different level of atmospheric perturbations. The phase map where simulated with HCIPy, a framework written in Python for high contrast imaging simulation (Por et al. 2018). The atmospheric residuals are obtained by simulation of a closed-loop adaptive optics system, based on the the Spectro-Polarimetric

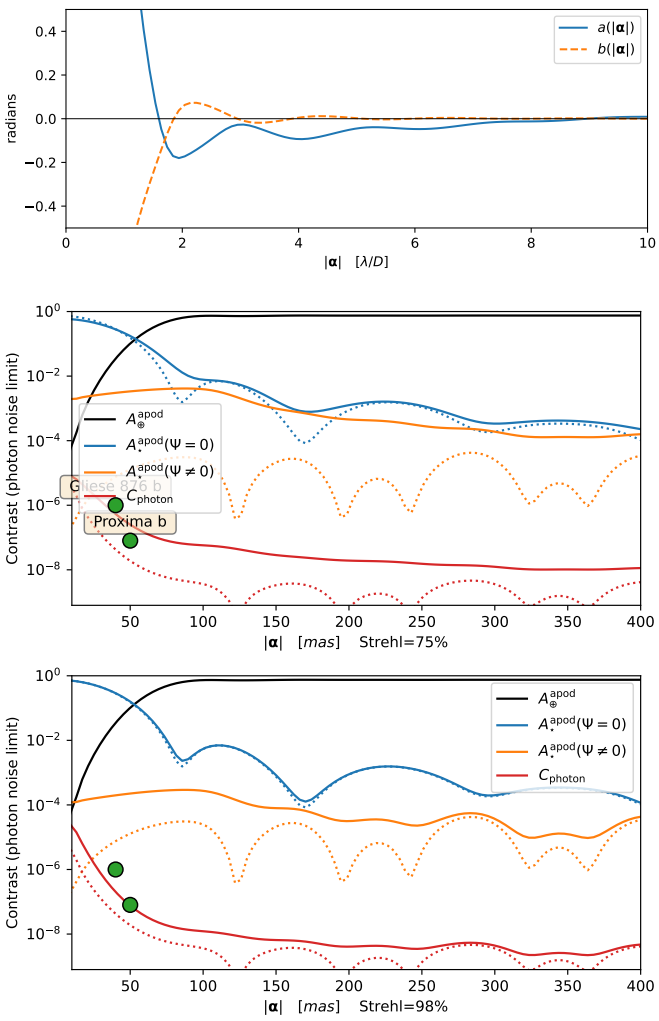

Fig. 3. *Upper panel:* the apodizer parameters, as a function of $\boldsymbol{\alpha}$, the separation between the star and the planet. The parameters a and b are poportionality factors to 2 prescriptions, one in $\sin(k_0\boldsymbol{\alpha}\cdot\boldsymbol{u})$ and the other in $k_0\boldsymbol{\alpha}\cdot\boldsymbol{u}\cos(k_0\boldsymbol{\alpha}\cdot\boldsymbol{u})$. *Middle panel:* the apodization of the stellar flux as a function of α, as a function of the separation $\boldsymbol{\alpha}$. The atmospheric correction is modeled by a strehl of 75 %, limiting the extinction of the stellar light. Without apodizer, the 1 % of the stellar light enters the fiber at 100 mas. It is decrease to a few 10^{-3} when introducing phase apodiztion (solid orange curve compared). This apodization also affects the exoplanetary signal below 100 mas (black curve). The parameters of this simulation are given in Table 2, with as a red curve the final contrast that could be acheive when limited by the stellar photon noise only. *Lower panel:* same as middle panel but with a strehl of 98 %. The apodizer new decreases the stellar light by a factor 10^{-4}.

High-contrast Exoplanet REsearch (SPHERE) adaptive optics (AO) system, that uses a Shack-Hartmann WFS. The simulations includes WFS Photon Noise and Time Lag of the AO system. The middle panel shows a simulation made with a strehl of 75%, the lower panel with a strehl of 98%. The doted curves in both panels correspond to a system without atmosphere (Strehl of 100%).

The simulations assumed the default parameters for the VLTI (Table 2). The color curves correspond to the atenuations of the light injected into interferometer 2 for the exoplanet (in black) and the star. The blue curve shows the stellar flux in abscence of apodization ($\Psi(\boldsymbol{u}) = 0$) while the orange curve shows the flux with an apodized mask as computed from Eq. (25) and using

the values in the upper panel of Figure. 3. In red, we plot the contrast limation purely due to photon noise. It can be obtained by inversion of the Eq. (11) simplified to:

$$snr_{\text{photon}} = \frac{S_\oplus A_\oplus^{\text{apod}}}{\sqrt{S_\star A_\star^{\text{apod}}}} \tag{26}$$

or, by introducing C_{photon} the ratio between $S_\star$ and $S_\oplus$ at a $snr_{\text{photon}} = 1$:

$$C_{\text{photon}} = \frac{\sqrt{A_\star^{\text{apod}}}}{\sqrt{S_\star} A_\oplus^{\text{apod}}} \tag{27}$$

This plots shows that the contrast, limited by photon noise, is barely sufficient to detect the 2 exoplanets Gliese 876b and Proxima b in the K band. According to these simulations, obtaining a stellar extinction of the order of 1e-4 is primordial if one want to be able to observe exoplanet with contrast ratio of the order of 1e-7. Hence, for this to work, a very good Strehl value is required because otherwise it is impossible for pupil apodization to extinguish at a sufficient depth the stellar light.

2.4. Coherent speckle removal

Because of the chromaticity behavior of the stellar light, and because of residual quasi-static aberrations, the apodizer cannot decrease the stellar light so that the coherent speckles completely diseapear. It is therefore necessary to filter them out.

This removal is based on the fact that we are simultaeously observing the stellar light on 2 optical inteferometers. We mesure on interferometer 1 a coherent flux, $\langle E_{T_1,I_1,\star} E^*_{T_2,I_1,\star}\rangle$. This coherent flux is phased on the stellar coherent speckle observed on interferometer 2, $\langle E_{T_1,I_1,\star} E^*_{T_2,I_1,\star}\rangle$. This is thanks to internal monitoring of the non common optical path (using the metrology as described in Fig. 1). Mathematically it can write as:

$$\langle E_{T_1,I_2,\star} E^*_{T_2,I_2,\star}\rangle \approx\propto \langle E_{T_1,I_1,\star} E^*_{T_2,I_1,\star}\rangle\,. \tag{28}$$

Which means that :

1. the amplitude of the coherent flux observed on the first interferometer has a similar spectral shape as the amplitude of the coherent speckle on the second interferometer.
2. the phase slope of the coherent flux observed on the first interferometer is not very different from the phase slope of the coherent speckle on the second interferometer.

But the best part of using a metrology system is that it is also possible to predict analytically the expected exoplanet complex coherent flux from the observation of the coherent energy on interferometer 1, assuming we know $\boldsymbol{\alpha}$ and $\mathsf{S}_\oplus/\mathsf{S}_\star$, respectively the angular separation and the contrast ratio between the planet and the star. This can be analytically demonstrated from the electric fields described in Table 1:

$$\langle E_{T_1,I_2,\oplus} E^*_{T_2,I_2,\oplus}\rangle = \frac{\mathsf{S}_\oplus}{\mathsf{S}_\star}\langle E_{T_1,I_2,\star} E^*_{T_2,I_2,\star}\rangle \exp(-ik\boldsymbol{\alpha}\cdot\boldsymbol{B})\,. \tag{29}$$

Thus, it is possible to filter the coherent speckles $\langle E_{T_1,I_2,\star} E^*_{T_2,I_2,\star}\rangle$ out of the coherent signal $\langle E_{T_1,I_2,\star} E^*_{T_2,I_2,\star}\rangle + \langle E_{T_1,I_2,\oplus} E^*_{T_2,I_2,\oplus}\rangle$ by knowing the fact that $\langle E_{T_1,I_2,\oplus} E^*_{T_2,I_2,\oplus}\rangle$ is modulated in wavelength by a function $\exp(-ik\boldsymbol{\alpha}\cdot\boldsymbol{B})$ while $\langle E_{T_1,I_2,\star} E^*_{T_2,I_2,\star}\rangle$ is not modulated. More exactly, assuming that $\boldsymbol{\alpha}$, the position of the planet, is known from Gaia astrometry for exemple, the goal of the postprocessing algorithm is hence to retreive a single parameter, $C = \mathsf{S}_\oplus/\mathsf{S}_\star$, which is a proportionality factor between two complex vectors as a function of wavelength, $\langle E_{T_1,I_1,\star} E^*_{T_2,I_1,\star}\rangle$ and $\langle E_{T_1,I_2,\oplus} E^*_{T_2,I_2,\oplus}\rangle$.

The ExoGRAVITY collaboration post processing technique, pionnered in GRAVITY Collaboration et al. (2019), and described in appendix of GRAVITY Collaboration et al. (2020) uses a specific filtering technique that is used here to estimate N_{speckle}. The filtering technique to retreive $\mathsf{S}_\oplus/\mathsf{S}_\star$ consists in 2 steps: the first step is to project the coherent flux in a subspace orthogonal to the subspace of the coherent speckle. This subspace is defined by a series of vectors J_n and Q_n. These vectors are a combination of polynomial vectors of lambda, multiplied by the complex vector $\langle E_{T_1,I_1,\star} E^*_{T_2,I_1,\star}\rangle$:

$$J_n = \lambda^n \times \langle E_{T_1,I_1,\star} E^*_{T_2,I_1,\star}\rangle \tag{30}$$

$$Q_n = i\lambda^n \times \langle E_{T_1,I_1,\star} E^*_{T_2,I_1,\star}\rangle \tag{31}$$

The second step is to project the coherent flux in the subspace defined by the theoretical position of the exoplanet. This subspace is strictly defined by a single vector K. It assumes that the angular separation $\boldsymbol{\alpha}$ is already known:

$$K = \langle E_{T_1,I_2,\star} E^*_{T_2,I_2,\star}\rangle \exp(-ik\boldsymbol{\alpha}\cdot\boldsymbol{B})\,. \tag{32}$$

Hence, while we already have spelled in Eq (13) the exoplanetary signal as:

$$S_\oplus A_\oplus^{\text{apod}} = \left\|\langle E_{T_1,I_2,\oplus} E^*_{T_2,I_2,\oplus}\rangle\right\|\,, \tag{33}$$

we can similarly spell the strength of the exoplanetary signal after postprocessing as:

$$S_\oplus A_\oplus^{\text{apod}} A_\oplus^{\text{processing}} = \left\|\text{proj}_K(\text{oproj}_{J_n,Q_n}\langle E_{T_1,I_2,\oplus} E^*_{T_2,I_2,\oplus}\rangle)\right\| \tag{34}$$

where "proj_K" means a projection on the vector K:

$$\text{proj}_K A = \frac{A\cdot K}{\|K\|^2} K \tag{35}$$

and "oproj_{J_n,Q_n}" means a projection on the subspace orthogonal to the J_n and Q_n vectors:

$$\text{oproj}_{J_n,Q_n} A = A - \sum_n \frac{A\cdot J_n}{\|J_n\|^2} J_n - \sum_n \frac{A\cdot Q_n}{\|Q_n\|^2} Q_n\,. \tag{36}$$

Hence, we can compute the theoretical atenuation of the exoplanetary signal by postprocessing as:

$$A_\oplus^{\text{processing}} = \frac{\left\|\text{proj}_K(\text{oproj}_{J_n,Q_n}\langle E_{T_1,I_2,\oplus} E^*_{T_2,I_2,\oplus}\rangle)\right\|}{\left\|\langle E_{T_1,I_2,\oplus} E^*_{T_2,I_2,\oplus}\rangle\right\|} \tag{37}$$

Similarly, the attenuation of the coherent stellar speckle can be writen as:

$$A_\star^{\text{processing}} = \frac{\left\|\text{proj}_K(\text{oproj}_{J_n,Q_n}\langle E_{T_1,I_2,\star} E^*_{T_2,I_2,\star}\rangle)\right\|}{\left\|\langle E_{T_1,I_2,\star} E^*_{T_2,I_2,\star}\rangle\right\|} \tag{38}$$

which contribute to a remaining coherent flux which are the coherent speckle residual after postprocessing:

$$N_{\text{speckle}} = S_\star A_\star^{\text{apod}} A_\star^{\text{processing}} \tag{39}$$

In Fig. 4 are ploted the attenuation of the exoplanet signal $A_\oplus^{\text{apod}} A_\oplus^{\text{processing}}$ as a function of angular separation for the parameters mentionned in Table 2. Representated are three level

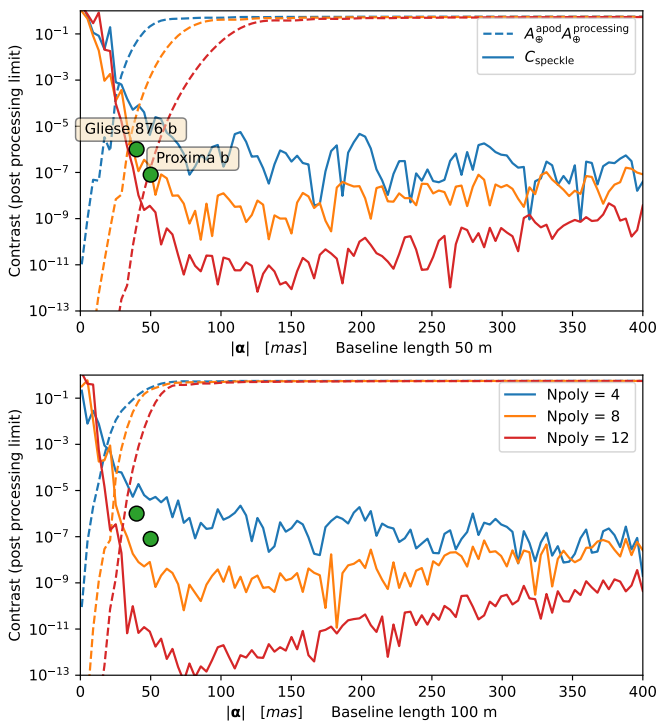

Fig. 4. The three colors correspond to three degrees of polynomial fitting (either 4, 8 or 12). The upper plot correspond to an observation with a baseline of 50 m, while the lower plot correspond to an observation of with a 100 m interferometer. *Dotted curves :* attenuation of the exoplanet signal $A_\oplus^{apod} A_\oplus^{processing}$ as a function of the angular separation for the parameters mentionned in Table 2. The smaller the order of the polynomial, the lower the inner working angle. *Solid curves :* contrast limit from post-postprocessing of the stellar speckle ($A_\star^{apod} A_\star^{processing} / A_\oplus^{apod} A_\oplus^{processing}$). The higher the order of the polynomial, the lower the contrast limit ist.

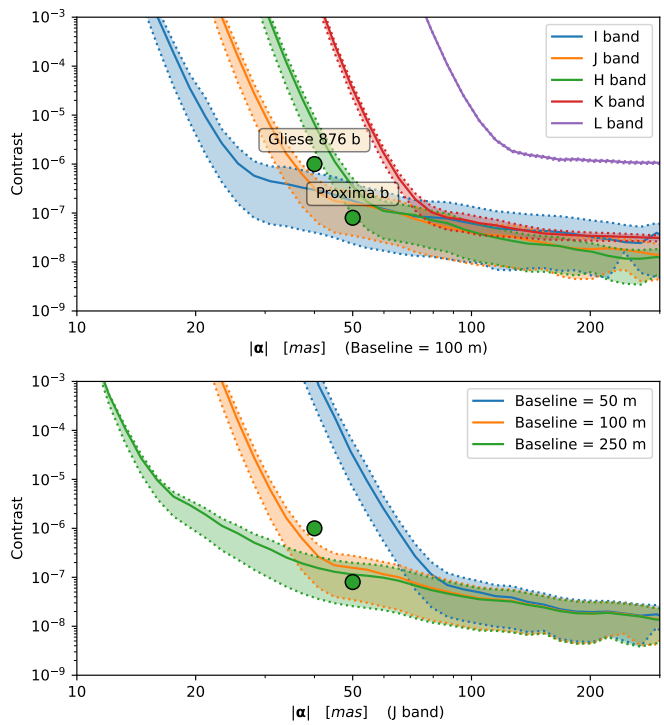

Fig. 5. Contrast limit as a function of angular separation. The parameters of the simulations are given in Table 2. The upper panel shows the dependance of the contrast as function of the waveband, for a given baseline of 100 m. The lower panel shows the contrast limit for different baseline lenght, assuming observations in the J band. The shadded aera correspond to different sthrel ratio, from 75 % for the upper limits, to 98 % for the lowest contrast limit. The inner working angle is limited by the telescope point spread function and by the interferometric resolution. The contrast range of the K and L band is limited by the thermal background.

of strengh for the deconvolution, N_{poly} of 4, 8 and 12, which correspond to the number of polynomials used to creates the J_n and Q_n vectors. Two baseline lengths were assumed for this deconvolution, either 50 m or 100 m, which correspond to the typical maximum baseline length accessible with the VLTI: 50 meters in the North-West direction, and 100 meters for North-East direction.

We also show the contrast limit only due to the strength of the coherent speckle after post processing. It can be obtained by inversion of the Eq. (11) simplified to:

$$snr_{speckle} = \frac{S_\oplus A_\oplus^{apod} A_\oplus^{processing}}{S_\star A_\star^{apod} A_\star^{processing}} \tag{40}$$

and by introducing $C_{speckle}$ the ratio between $S_\star$ and $S_\oplus$ at a $snr_{speckle}$ of 1:

$$C_{speckle} = \frac{A_\star^{apod} A_\star^{processing}}{A_\oplus^{apod} A_\oplus^{processing}} \tag{41}$$

Last, we plotted the two most favorable targets Gliese 876 b and Proxima Centuri b. In the context of an instrument purely limited by the speckle noise, the two exoplanets would be difficult to detect on the small baseline, but doable on the longuest thanks to the larger inner working angle.

2.5. Contrast curve

All these sources of noise described in the previous paragraphs can combined to create a final contrast range that is obtained thanks to the inversion of Eq. (11). Assuming the contrast limit is given for a signal to noise of 1 sigma, the contrast limit can be written as:

$$C = \frac{\sqrt{N_{readout}^2 + N_{background}^2 + S_\star A_\star^{apod} + (S_\star A_\star^{apod} A_\star^{processing})^2}}{S_\star A_\oplus^{apod} A_\oplus^{processing}} \tag{42}$$

The resulting contrast is plotted in Fig. /reffig:Cfull. An important parameter is the inner working angle. This inner working angle is limited by the pupil apodizer (at λ/D) and by the speckle filtering (around $10\lambda/B$), whichever is smaller. Therefore, it is no surprise that the wavelength, λ, is a fundamental parameter of the inner working angle. The upper panel of Fig. /reffig:Cfull is illustrative of that effect: a contrast range of 10^6 can be obtained at 20 mas in the I band, but only at 70 mas in the K band. Reducing the baseline by a factor 2 would also increase the working inner angle by a factor 2, as seen in the lower panel. It is noteworthy to see that it is also possible to decrease the inner working by increasing the baseline above what is acheivable by the VLTI.

The strehl is also playing a predominant role. It has an effect both on the signal injected inside the fiber, and on the amont of apodization of the stellar flux (see Fig 3). The shaded array in

the Fig. /reffig:Cfull. correspond to a range of strehl between 75 and 98 percents defined in the K band. At 100 mas, the strehl is what makes the contrast limit going from 1e-7 to 1e-8. It is therefore paramont for the discovery space. It is interesting to note that at shorter wavength, the effect of the strehl does not make things worse, because it is conterbalanced by other effect, like a improvement of stellar attenuation thanks to the higher resolution.

Last we can see that observing reflected light of exoplanets above 2 microns would be defficault, because of background noise. A possibility could be to target thermal emmission of exoplanets, but that may need a cold environment, where space would excel.

Acknowledgements. This research made use of HCIPy, an open-source object-oriented framework written in Python for performing end-to-end simulations of high-contrast imaging instruments (Por et al. 2018).

References

Baker, N. 1966, in Stellar Evolution, ed. R. F. Stein,& A. G. W. Cameron (Plenum, New York) 333
Balluch, M. 1988, A&A, 200, 58
Cox, J. P. 1980, Theory of Stellar Pulsation (Princeton University Press, Princeton) 165
Cox, A. N.,& Stewart, J. N. 1969, Academia Nauk, Scientific Information 15, 1
Mizuno H. 1980, Prog. Theor. Phys., 64, 544
Tscharnuter W. M. 1987, A&A, 188, 55
Terlevich, R. 1992, in ASP Conf. Ser. 31, Relationships between Active Galactic Nuclei and Starburst Galaxies, ed. A. V. Filippenko, 13
Yorke, H. W. 1980a, A&A, 86, 286
Zheng, W., Davidsen, A. F., Tytler, D. & Kriss, G. A. 1997, preprint